Journal of Materials Science & Technology 159 (2023) 204–218

Contents lists available at ScienceDirect

Journal of Materials Science & Technology

journal homepage: www.elsevier.com/locate/jmst

Research Article

Dislocation mediated dynamic tension-compression asymmetry of a $Ni_2CoFeV_{0.5}Mo_{0.2}$ medium entropy alloy

Ao Meng[a], Xiang Chen[a,*], Yazhou Guo[b], Yiping Lu[c,*], Yonghao Zhao[a,*]

[a] Nano and Heterogeneous Materials Center, School of Materials Science and Engineering, Nanjing University of Science and Technology, Nanjing 210094, China
[b] School of Aeronautics, Northwestern Polytechnical University, Xi'an 710072, China
[c] Key Laboratory of Solidification Control and Digital Preparation Technology (Liaoning Province), School of Materials Science and Engineering, Dalian University of Technology, Dalian 116024, China

ARTICLE INFO

Article history:
Received 21 July 2022
Revised 11 December 2022
Accepted 7 February 2023
Available online 13 April 2023

Keywords:
Medium entropy alloy
Dynamic deformation
Tension-compression asymmetry
Slip trace analysis
EBSD and TEM

ABSTRACT

Although tension-compression (T-C) asymmetry in yield strength was rarely documented in coarse-grained face centered cubic (FCC) metals as critical resolved shear stress (CRSS) for dislocation slip differs little between tension and compression, the T-C asymmetry in strength, i.e., higher strength when loaded in compression than in tension, was reported in some FCC high entropy alloys (HEAs) due to twinning and phase transitions activated at high strain regimes in compression. In this paper, we demonstrate a reversed and atypical tension-compression asymmetry (tensile strength markedly exceeds compressive strength) in a non-equiatomic FCC $Ni_2CoFeV_{0.5}Mo_{0.2}$ medium entropy alloy (MEA) under dynamic loading, wherein dislocation slip governs dynamic deformation without twins or phase transitions. The asymmetry can be primarily interpreted as higher CRSS and more hard slip modes (lower average Schmid factor) activated in grains under dynamic tension than compression. Besides, larger strain rate sensitivity in dynamic tension overwhelmingly contributes to the higher flow stress, thanks to the occurrence of more immobile Lomer-locks, narrower spacing of planar slip bands and higher dislocation density. This finding may provide some insights into designing MEAs/HEAs with desired properties under extreme conditions such as blast, impact and crash.

1. Introduction

Definite tension-compression (T-C) asymmetry, in terms of both yield strength and ultimate strength, was widely reported in hexagonal closed packed (HCP) materials subjected to deformation [1–9]. For HCP materials with low symmetry nature, the T-C asymmetry can be exceedingly pronounced. In general, the T-C asymmetry is intimately related to the asymmetry in the critical resolved shear stress (CRSS) of active deformation modes (e.g., dislocation slip and twinning) between tension and compression. First, the CRSS required to initiate the movement of dislocations is remarkably different for the different slip systems in HCP materials, respectively [3,6]. Taking pure Mg as an exemplar, the CRSS for non-basal slip is about 100-fold as that for basal slip [10]. Also, more frequent pyramidal $\langle c+a \rangle$ slip activity gives rise to a higher strength during compression, compared with that for tension of the textured Mg-5Y alloys [8]. Second, twinning activities depend strongly on the loading direction [11,12]. The stress required to activate the secondary extension twins (305 MPa) in tension is larger than that in compression (284 MPa), leading to the T-C asymmetry in the yielding of Ti [13]. Above all, the T-C asymmetry in yield strength is intimately related with the CRSS anisotropy with respect to the loading direction and initial grain orientations.

Compared with HCP materials, the T-C asymmetry was sporadically documented in coarse-grained face centered cubic (FCC) metals such as Al, Cu and Ni, due to their high symmetry and weak CRSS anisotropy for different slip systems [14,15]. However, the T-C asymmetry in flow strength, i.e., higher strength when loaded in compression than in tension, was recently reported in some FCC high entropy alloys (HEAs) [16,17]. HEAs have garnered tremendous attention for their immense structural diversity and linked properties, including remarkable fracture toughness [18–20], high strength [21–25] and good ductility [26–30]. As to the T-C asymmetry, Joseph et al. [16] revealed the exceptionally high work hardening ability in quasi-static compression of $Al_{0.3}CoCrFeNi$ is attributed to profuse mechanical twinning, in contrast to the tensile sample deformed solely by dislocation slip. An et al.

* Corresponding authors.
E-mail addresses: xiang.chen@njust.edu.cn (X. Chen), luyiping@dlust.edu.cn (Y. Lu), yhzhao@njust.edu.cn (Y. Zhao).

https://doi.org/10.1016/j.jmst.2023.02.051
1005-0302/

[17] demonstrated that phase transformation from FCC to HCP structure plays a paramount role in elevating the compressive stress of $Fe_{40}Co_{20}Cr_{20}Mn_{10}Ni_{10}$, while this mechanism is negligible under tension. Overall speaking, the T-C asymmetry in flow strength is strongly dependent on the activation of three dominant mechanisms in different work hardening stages: dislocation activities, twins and phase transitions.

Previous investigations of HEAs pointed out that high strain rate (HSR) is deemed favorable for the activation of twinning and phase transitions, even for amorphization in extreme deformation [31–43]. For instance, a superior combination of strength and ductility was attained under dynamic compression of $Al_{0.6}CoCrFeNi$ HEAs, thanks to the activation of deformation twins and abundant dislocations [31]. Quantitative microstructural analysis deciphered that the cooperation of twins and dislocations was responsible for the synchronous enhancement of strength-plasticity and hydrogen-retarded spallation in CrMnFeCoNi HEA under dynamic tension and compression [44]. In addition, transitions from FCC to BCC/HCP structure and amorphization were experimentally observed in VCrFeCoNi and CrMnFeCoNi HEAs subjected to dynamic tension [40,42]. Transitions from slip and twinning to solid-state amorphization were also verified via molecular dynamics simulations of CoCrNi MEA [45]. Although a myriad of deformation mechanisms was anticipated in the high strain rate regime, dynamic loading of the HEAs remains largely unexplored, not to mention that the difference between dynamic tension and compression of HEAs has never been examined before.

In the present work, a non-equiatomic FCC $Ni_2CoFeV_{0.5}Mo_{0.2}$ MEA with moderate stacking fault energy (SFE) about 50 mJ m^{-2} was chosen to systematically investigate the mechanical response and subsequent microstructural alterations subjected to both dynamic tension and compression. Our research focus is therefore to uncover the T-C asymmetry behavior and decipher the underlying mechanisms in the present MEA, in an effort to explore its untapped potential of utilization under extreme environments.

2. Experimental

2.1. Sample preparation

The as-cast ingot with the nominal composition of $Ni_2CoFeV_{0.5}Mo_{0.2}$ was fabricated by a medium frequency vacuum induction melting furnace. Ni, Co, Fe, V and Mo elements were employed with purities greater than 99.5%. These elements were put into the BN crucible. Prior to the melting process, the furnace chamber was evacuated to 10^{-2} Pa under a protective argon atmosphere to 0.06 MPa. The liquid metal maintained at 1823 K for 15 min was then poured into a ZrO_2-coated MgO crucible (preheated at 873 K before casting). The temperature was recorded by an IRTM-2CK infrared pyrometer with an absolute accuracy of 2 K. The desired alloy was re-melted and flipped three times in an effort to attain homogeneity. The cylindrical cast ingot was approximately 60 mm in diameter and 130 mm in height.

2.2. Dynamic tensile and compressive testing

A series of tension and compression tests were conducted on the samples cut along the height direction (Fig. 1) inside the as-casted ingot. Cubic compression specimens with a dimension of 5 mm × 5 mm × 5 mm were sectioned by electrical discharge machining (EDM) and cylindrical tension specimens with a dimension of Φ5 mm × 3 mm were turned by the numerically controlled lathe. All compression specimens were polished to be mirror-like for the ex-situ observation carefully using a diamond suspension with a particle size of 0.25 μm. It is worth noting that all the bulk specimens were subjected to ex-situ characterization and at least three samples were tested in order to ensure reproducibility. The dynamic compression and tension samples were performed using the Split Hopkinson Pressure Bar (SHPB) and Split Hopkinson Tension Bar (SHTB) with strain rates of 1000, 2000, and 3000 s^{-1} (the details in Fig. S1 in Supplementary Information). The dynamic stress was measured by the strain gauges on the incident and transmitted bars. The strain rate, $\dot{\varepsilon}$, true strain, ε, and true stress, σ, can be obtained by the following equations [46].

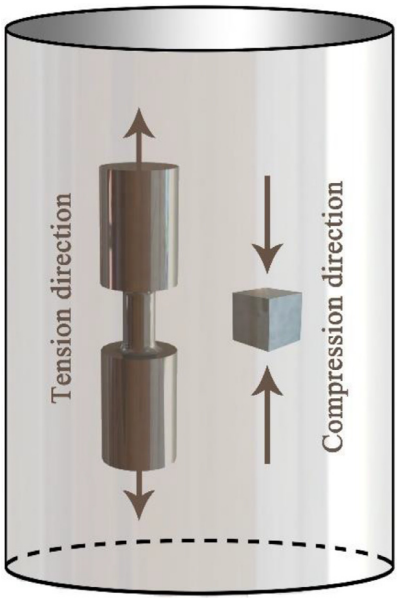

Fig. 1. Schematic illustration of the as-casted ingot and the loading direction of the samples subjected to dynamic tension and compression.

$$\dot{\varepsilon} = -\frac{2C_0}{L_0}\varepsilon_r(t) \quad (1)$$

$$\varepsilon = -\frac{2C_0}{L_0}\int_0^l \varepsilon_r(t)\mathrm{d}t \quad (2)$$

$$\sigma = \frac{A_0}{A}E\varepsilon_t(t) \quad (3)$$

where E is the elastic modulus of the incident and transmission bars, A_0 and L_0 refer to the initial cross-sectional area and length, respectively, A is the cross-sectional area of the incident and transmission bars, C_0 is the longitudinal wave velocity in the bars, and $\varepsilon_r(t)$ and $\varepsilon_t(t)$ are the experimentally measured strains of the incident and transmitted stress pulses on the split-Hopkinson bars, respectively.

2.3. Microstructural characterizations

Microstructures were characterized by means of scanning electron microscopy (SEM, Quanta 250 F, FEI, Hillsboro, OR, USA), electron back-scattered diffraction (EBSD), transmission electron microscopy (TEM) and high-resolution transmission electron microscopy (HRTEM) techniques. All the microstructures were observed on the plane of the specimens parallel to the tension or compression direction (see Fig. S2 for details). Phase constitution was examined by X-ray diffraction (XRD, D8, Bruker, Coventry, Germany). The EBSD mapping was obtained using high-resolution field emission SEM (Carl Zeiss-Auriga-45–66) equipped with a fully automatic Oxford Instruments Aztec 2.0 EBSD system (Channel 5 software). The EBSD specimens were mechanically polished with SiC paper and then electro-polished in an electrolyte containing 90 vol.% acetic acid and 10 vol.% perchloric acid using a voltage

of 35 V and polishing time of 50 s in a Buehler ElectroMet 4 polisher. The surface slip trace distribution after dynamic deformation was analyzed by using Spyder and MATLAB with MTEX codes [47]. TEM and HRTEM observations were conducted in FEI-Tecnai G^2 20 S-TWIN and Titan G2 60–300 microscopes operated at 200 and 300 kV, respectively. The TEM and HRTEM specimens were ground down to 60 μm thickness, punched into 3 mm diameter discs and then electro-polished in an aqueous electrolyte containing 25 vol.% perchloric acid, and 75 vol.% acetic acid at 20 °C via a twin jet electro-polishing system. The atom probe tomography (APT) test was carried out with a local electrode atom probe (LEAP 4000X Si) under ultraviolet laser pulsing at a laser energy of 40 pJ, a pulse repetition rate of 200 kHz, and a detection rate of 0.5% at 40 K. The IVAS 3.6.8 software was used for data reconstruction and quantitative analysis.

3. Results

3.1. Initial microstructural characterization

According to the EBSD mapping (Fig. 2(a)), the as-cast $Ni_2CoFeV_{0.5}Mo_{0.2}$ sample is composed of randomly orientated grains with a mean grain size of 520 ± 275 μm and the percentage of high angle grain boundaries (HAGBs) is ~77.5%. The XRD pattern at the bottom of Fig. 2(a) confirms the single FCC solid solution. The APT elemental maps of the MEA in Fig. 2(b) show that the distribution of Ni, Co, Fe, V, and Mo appears to be random at the nanometer scale. The table in Fig. 2(b) shows the measured composition is close to the nominal one.

3.2. Dynamic tensile and compressive properties

Fig. 3 shows the true stress-strain and corresponding strain hardening rate curves of the $Ni_2CoFeV_{0.5}Mo_{0.2}$ MEA under both tension and compression for different strain rates at room temperature. The observed oscillation in the dynamic stress–strain curve is generally at strains less than 0.05, arising from elastic wave dispersion in the pressure bars. For the dynamic deformed samples (Fig. 3(a) and (c)), the shape of the true stress-strain curves is generally linear. Moreover, for the dynamic compressive samples after yielding, no precipitous stress drop is recorded, indicating strong resistance against plastic instability. The dynamic compressive YS is 340 ± 13, 356 ± 20, and 372 ± 21 MPa at the strain rate of 1000, 2000, and 3000 s^{-1}, respectively. While for dynamic tension, the YS is 408 ± 8, 489 ± 6, and 510 ± 66 MPa at the strain rate of 1000, 2000, and 3000 s^{-1}, respectively. Note that the yield point is determined by the intersection of bilinear fitting curves of the elastic stage and the initial plastic flow stage.

Work hardening can be assessed by the strain hardening rate ($\Theta = \partial\sigma/\partial\varepsilon$, where σ is true stress, ε is true strain) within three distinct stages (Fig. 3(b), (d) and (f)). In stage I, the Θ descends rapidly due to the conventional transition from elastic deformation to slip-dominated plastic deformation for all the strain rates. For dynamic deformation in the beginning of stage II, the Θ increases for both tension and compression, but the Θ is higher in tension at strain rates of 1000 and 2000 s^{-1} (Fig. 3(b) and (d)). The Θ reaches a broad peak and decreases slightly in tension, while the Θ increases monotonously in compression at 3000 s^{-1} (Fig. 3(f)). The fluctuation of Θ at stage II may stem from elastic wave dispersion in the pressure bars for both dynamic tension and compression. In the last stage III, Θ decreases again at all strain rates due to the artificial stop of the experiment. The broad Θ peak of the MEA indicates excellent strain hardening ability at high strain rates.

The YS increases with the loading strain rate under both dynamic compression and tension and the YS is higher under dynamic tension (Fig. 4(a) and Table 1). Strain-rate sensitivity (SRS) is a vital parameter to characterize the strain-rate effect on the deformation of various metals. The value of the strain-rate sensitivity can be calculated as [46]:

$$m = \left(\frac{\partial 1n\sigma_y}{\partial 1n\dot{\varepsilon}}\right)_{\varepsilon,T} \tag{4}$$

where $\dot{\varepsilon}$ is the strain rate and σ_y is the yield stress. The average m value is measured to be 0.2098 and 0.0813 for the current MEA under dynamic tension and compression, respectively (Fig. 4(b) and Table 1). The high SRS was proposed as the phonon drag effect on the motion of dislocation, which propagates in the crystal as an elastic lattice vibration and interacts with the dislocations and becomes pronounced for HEAs/MEAs, leading to an increase in viscosity of dislocation movement at high strain rates [35,36]. The strain hardening exponent n can be obtained by the Ludwick equations, as shown below [48]:

$$\sigma = \sigma_0 + K\varepsilon_f^n \tag{5}$$

where σ_0 is the yield stress, ε_f is the true plastic strain, and K is the strength coefficient. The strain hardening exponent n increases with the increasing strain rate for dynamic compression, while the trend is inverse from 1000 s^{-1} to 2000 s^{-1} and keeps plateau from 2000 s^{-1} to 3000 s^{-1} for dynamic tension (Fig. 4(c) and Table 1). The minimum and maximum value of the strain hardening exponent is 1.15 ± 0.15, 1.47 ± 0.17 for dynamic tension at 3000 s^{-1} and compression at 2000 s^{-1}.

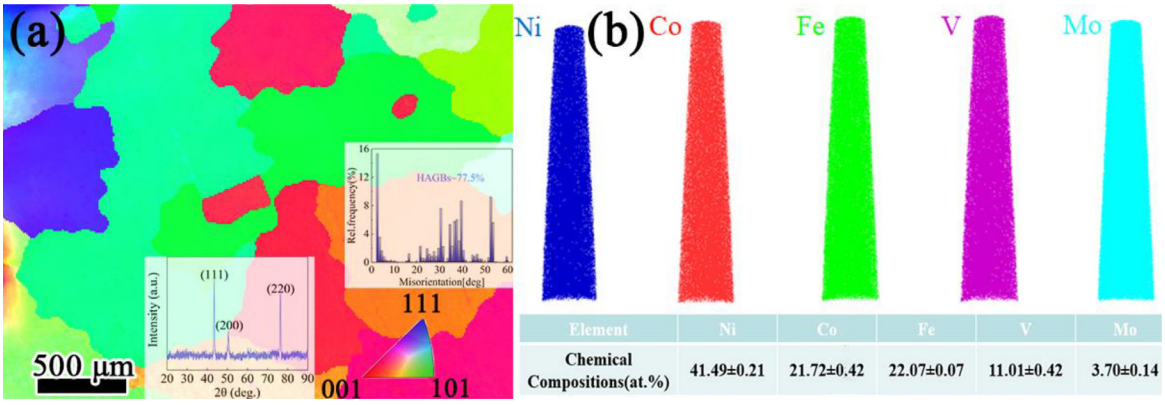

Element	Ni	Co	Fe	V	Mo
Chemical Compositions(at.%)	41.49±0.21	21.72±0.42	22.07±0.07	11.01±0.42	3.70±0.14

Fig. 2. Initial microstructures and compositional distributions of the $Ni_2CoFeV_{0.5}Mo_{0.2}$ MEA. (a) An EBSD orientation mapping of the MEA, with a histogram of grain boundary misorientation analysis inserted on the right of (a), and an XRD pattern inserted at the bottom of (a). The orientation is color coded based on the inset legend triangle; (b) APT analysis of Ni, Co, Fe, V, and Mo elements and measured chemical compositions in the MEA.

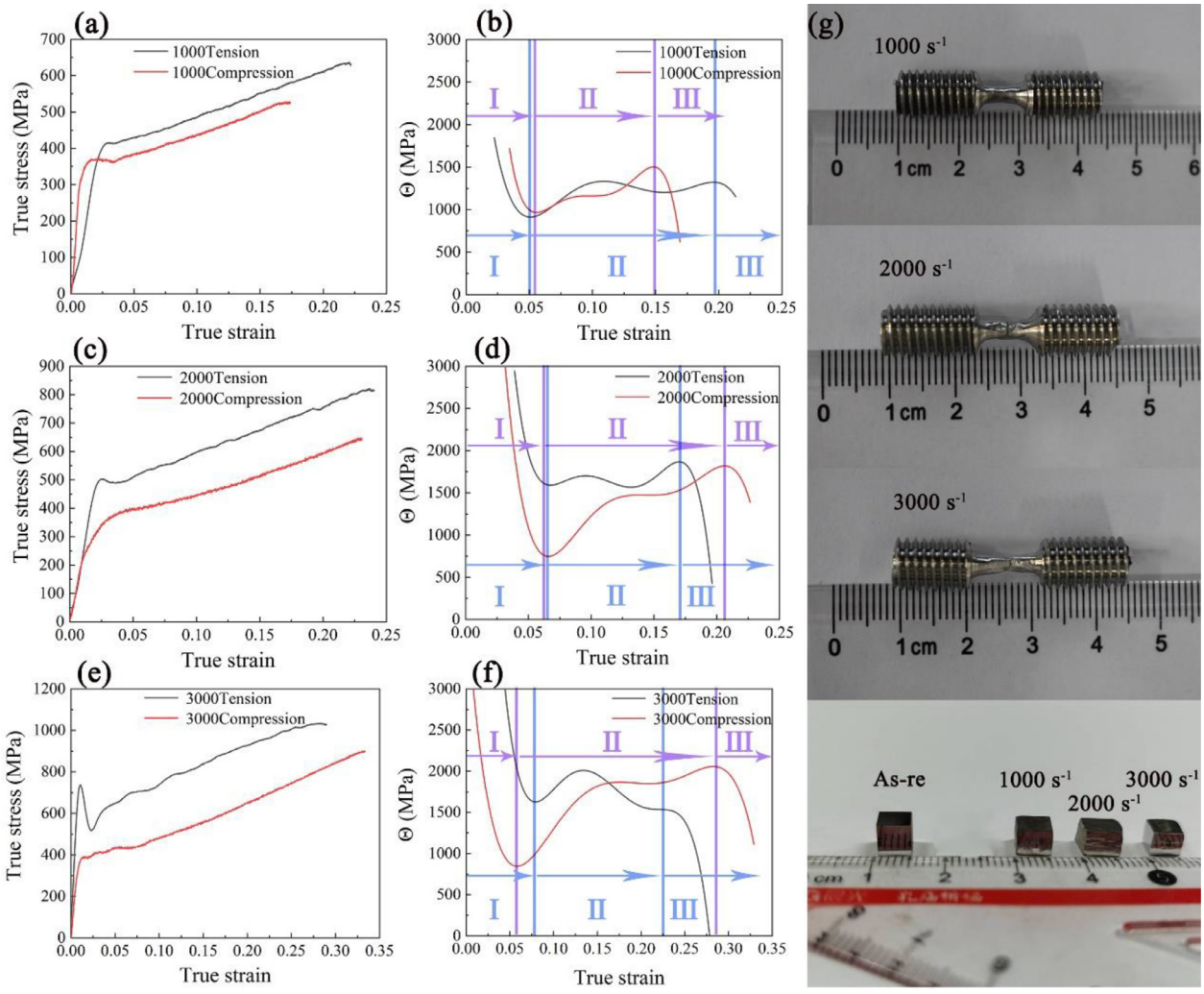

Fig. 3. True stress-stain curves and corresponding strain hardening rate curves of the $Ni_2CoFeV_{0.5}Mo_{0.2}$ MEA under both tension and compression at different strain rates: (a, b) 1000 s^{-1}; (c, d) 2000 s^{-1}; (e, f) 3000 s^{-1}. Noted that 1000 s^{-1} Tension - 3000 s^{-1} Compression would be called 1000Tension–3000Compression in the inset words of Fig. 3(a) to 3(f), respectively. The boundaries between the three stages for the strain hardening rate are represented by solid lines and arrows (blue lines and arrows for tension and purple lines and arrows for compression). In stage I, the Θ descends rapidly and the boundaries between stage II and stage III are determined by the trend of strain hardening rate, it is increasing or keeping plateau in stage II while decreasing monotonously in stage III. (g) Pictures of the deformed samples at each strain rate.

Table 1
Summary of yield stresses, strain-rate sensitivity, and average strain hardening exponent of the current MEA during dynamic deformation.

Dynamic deformation	Yield stress (MPa)	Strain-rate sensitivity	Average strain hardening exponent
Tension			
1000 s^{-1}	408 ± 8		1.35 35 ± 0.03
2000 s^{-1}	489 ± 6	0.2098	1.15 ± 0.20
3000 s^{-1}	510 ± 66		1.15 ± 0.15
Compression			
1000 s^{-1}	340 ± 13		1.22± 0.10
2000 s^{-1}	356 ± 20	0.0813	1.47 ± 0.17
3000 s^{-1}	372 ± 21		1.37± 0.16

Astonishingly, the tensile strength noticeably exceeds compressive strength under dynamic deformation (Fig. 4(d)), pointing to an unusual T-C asymmetry in the current MEA. To quantitatively evaluate the T-C asymmetry in terms of flow stress, the parameter $\Delta\sigma$ is defined as σ_T minus σ_C. Fig. 4(d) includes the T-C asymmetry reported for other HEAs and steels subjected to quasi-static (10^{-3} s^{-1}) and dynamic (2500 s^{-1}) loading, following the same trend: $\Delta\sigma < 0$. For instance, the $\Delta\sigma$ decreases from −48 MPa to −420 MPa as the strain increases to 0.3 for the $Fe_{40}Co_{20}Cr_{20}Mn_{10}Ni_{10}$ alloy at a strain rate of 10^{-3} s^{-1}. The $\Delta\sigma$ declines to −267 MPa at a strain of 0.3 for the Fe-1.0C-18Mn steel with a strain rate of 2500 s^{-1}. However, the T-C asymmetry is reversed ($\Delta\sigma > 0$) for the current MEA under different strain rates (Figs. 4(d) and S3). The value of $\Delta\sigma$ increases from 50 MPa to 280 MPa with the strain rate increasing from 1000 s^{-1} to 3000 s^{-1} at a strain of 0.17, holding the constant trend: $\Delta\sigma > 0$, in distinct contrast to the referenced materials.

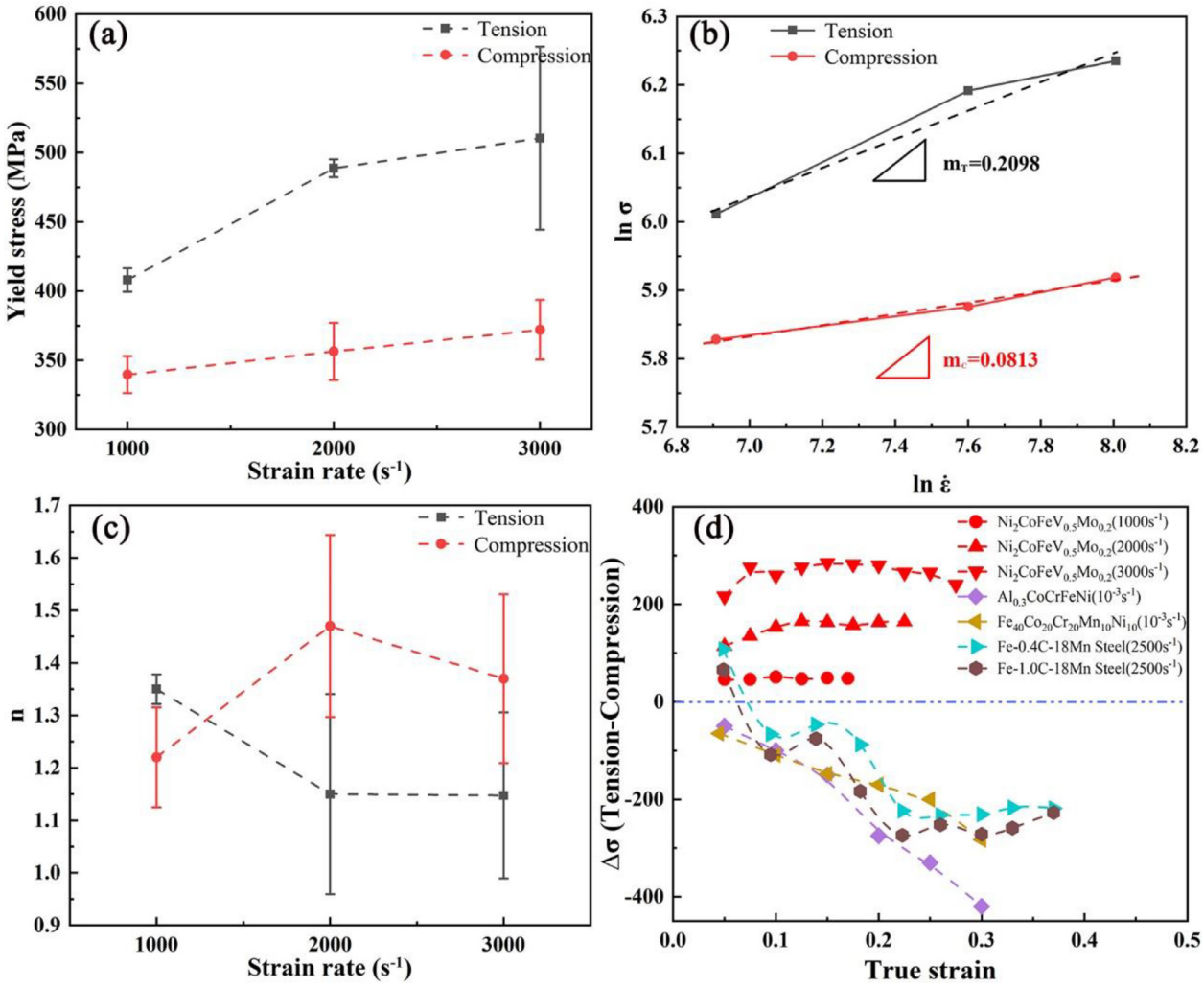

Fig. 4. (a) Variations of the yield stress with respect to the strain rates for the current MEA. (b) Variations of logarithmic yield stress with logarithmic strain rate. The *m* value is calculated based on the slope under dynamic tension and compression. (c) Strain hardening exponent under various strain rates. (d) Variations of $\Delta\sigma$ with the true strain for the current MEA and other HEAs and steels in the literature: $Al_{0.3}CoCrFeNi$, 10^{-3} s^{-1} [16]; $Fe_{40}Co_{20}Cr_{20}Mn_{10}Ni_{10}$, 10^{-3} s^{-1} [17]; Fe-0.4C-18Mn steel and Fe-0.4C-18Mn steel, 2500 s^{-1} [49].

3.3. Microstructure after dynamic tension and compression

The surface morphologies for the dynamic deformed samples were examined by SEM (see Fig. 5). For the tensile sample at 1000 s^{-1}, continuous slip takes place according to the lathe marks (reflected by the green dotted lines in Fig. 5(a)) perpendicular to the tensile direction. With the strain rate increasing to 2000 and 3000 s^{-1}, slip traces with multiple directions occur and cracks are initiated (Fig. 5(b) and (c)). Flaws and cracks are not detected under dynamic compression at each strain rate, indicative of strong resistance to adiabatic shear banding under compression. This stems from the high work hardening ability, analogous to the NiCoCrFe HEAs at high strain rates [50]. In addition, slip traces with multiple directions are observed for the samples at each compressive strain rate (Fig. 5(d–f)).

Microstructures of the deformed samples were examined by EBSD and TEM to understand the collective defect processes and the underlying mechanisms for the T-C asymmetry of strength. EBSD Inverse Pole Figure (IPF) maps show the structures consist of HAGBs and some sub-grains in the necking region for the 1000 s^{-1} tensile sample (Fig. 6(a)). In the side region (far away from the necking region), the slip traces can be captured in the coarse grains and the percentage of low-angle grain boundaries (LAGBs) is ~91.0% (Fig. 6(b)). Compared with the 1000 s^{-1} tensile sample, the necking side regions present similar microstructure at the strain rates of 2000 and 3000 s^{-1} (Fig. 6(c) and (e)), and the percentage of LAGBs is ~95.2% and ~89.4%, respectively (Fig. 6(d) and (f)). No twins and phase transformation are detected for all the tensile samples.

For the samples under dynamic compression, the grains are elongated perpendicular to the compression direction (Fig. 7(a), (c) and (e)). The elongated grains consist of a large volume fraction of LAGBs and a few HAGBs. The percentage of LAGBs is ~93.1%, ~92.7% and ~87.8% for the three samples, respectively (Fig. 7(b), (d) and (f)). Similarly, no mechanical twins and phase transitions occur under dynamic compression. In addition, for the sample subjected to quasi-static compression, the microstructure feature is similar to that of the dynamic compression samples (Fig. S3). Above all, dislocation slip is delineated to govern the defect processes during dynamic deformation of the current MEA.

As shown in the TEM image in Fig. 8(a), a few type slip traces and plenty of wavy dislocations form in the side region of the 1000 s^{-1} tensile sample. While in the side region of the 3000 s^{-1} tensile sample, planar slip predominantly occurs under a two-beam condition with the diffraction vector $\boldsymbol{g} = 200$ (Fig. 8(b)). Moreover, careful observation reveals that some sessile dislocations lie on {100} planes (marked by the green arrows in Fig. 8(a) and (b)), indicating that the gliding dislocations react on different {111} planes.

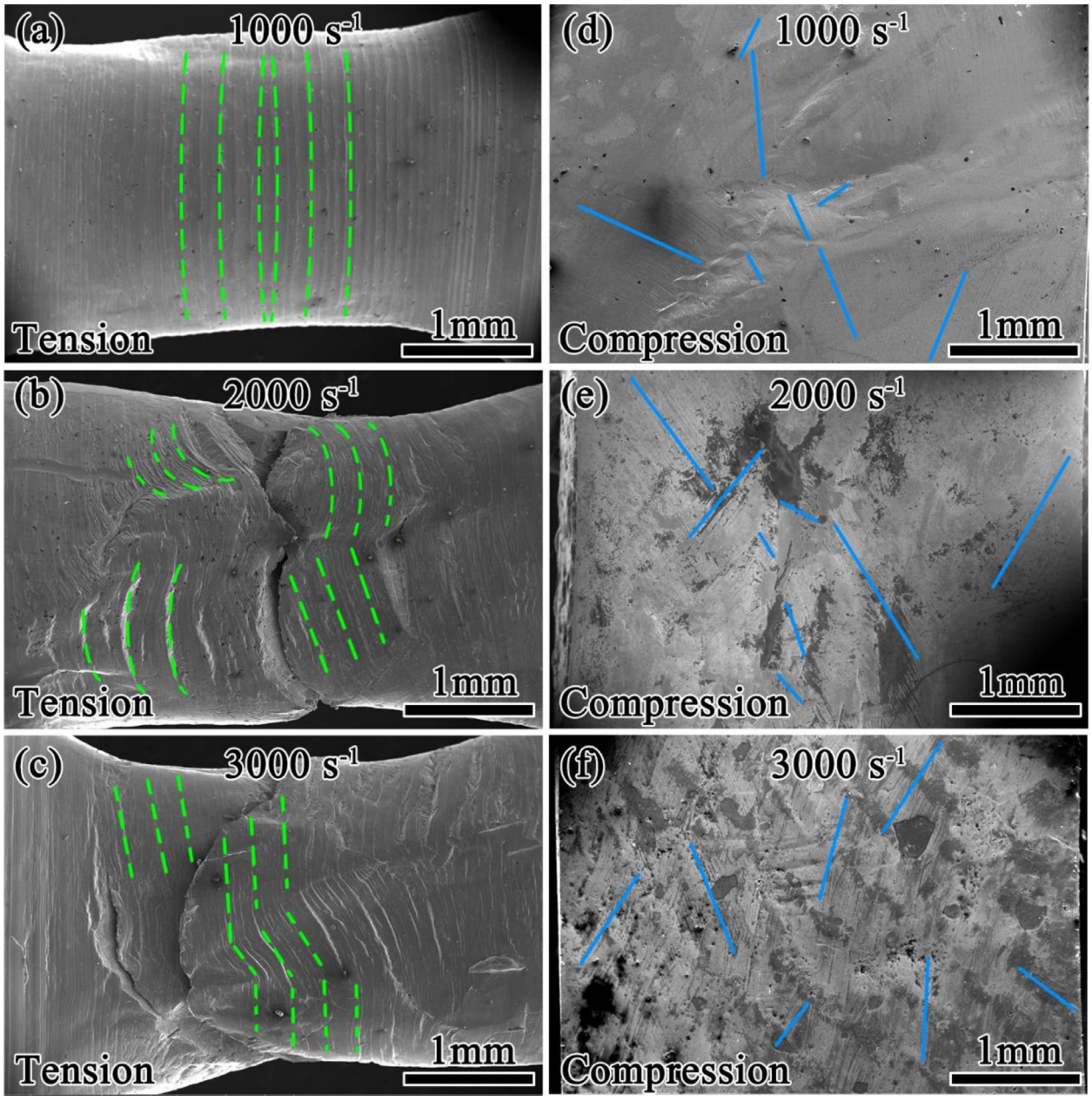

Fig. 5. SEM images of the samples under dynamic tension and compression at different strain rates: (a, d) 1000 s^{-1}; (b, e) 2000 s^{-1}; (c, f) 3000 s^{-1}. The green dotted lines reflect the slip trace for the dynamic tensile samples according to the lathe marks and solid lines represent the slip traces for the dynamic compressive samples.

The sessile dislocations known as the Lomer locks are formed by two full dislocation reactions: $\frac{a}{2}[011]+\frac{a}{2}[1\bar{1}0] \rightarrow \frac{a}{2}[101]$ (Fig. S4(a)). The resultant dislocations cannot lie on the {111} planes and are therefore immobile [51]. In the necking region of the 1000 s^{-1} and 3000 s^{-1} tensile samples, massive planar dislocation arrays and dislocation tangles are observed in a two-beam condition with $\boldsymbol{g} = 11\bar{1}$ near the [011] zone axis (Fig. 8(c) and (d)). Compared with the side regions, the distribution of the dislocations is more uniform and the dislocation density is higher. In addition, more than two variants of high dense dislocation walls (HDDWs) are clearly observed as indicated by yellow arrows in Fig. 8(c) and (d). HDDWs are dislocation substructures evolving from coplanar slip along {111} planes. It should be noted that the dominant mechanism is dislocation slip on {111} planes during dynamic tension. The spacing of the planar slip bands decreases from 125 ± 35 nm to 31 ± 17 nm in the necking regions with the strain rate increasing from 1000 s^{-1} to 3000 s^{-1} (see Fig. S4(b) and (c) for details). The higher strain rate gives rise to a tendency toward more planar networks and smaller spacing of the planar slip bands.

Under 1000 s^{-1} dynamic compression condition, samples deform primarily by dislocation glide and only two slip traces occur (indicated by blue lines in Fig. 8(e)) owing to the low strain of 0.17. Under a compressive strain rate of 3000 s^{-1}, the dislocations intersect each other and act as forest and HDDWs configuration at a high strain of 0.33 (Fig. 8(f)). The spacing of the planar slip bands decreases from 122 ± 42 nm to 64 ± 26 nm with the strain rate increasing from 1000 s^{-1} to 3000 s^{-1}. Neither twins nor phase transitions are discerned in quasi-static (Fig. S3), high strain rate compression, and even a higher strain rate of 8000 s^{-1} (see Fig. S5). In the current MEA, the T-C asymmetry should be intimately related with the dislocation-mediated processes, in contrast to the reported twinning or phase transition dependent T-C asymmetry in several existing HEAs [16,17].

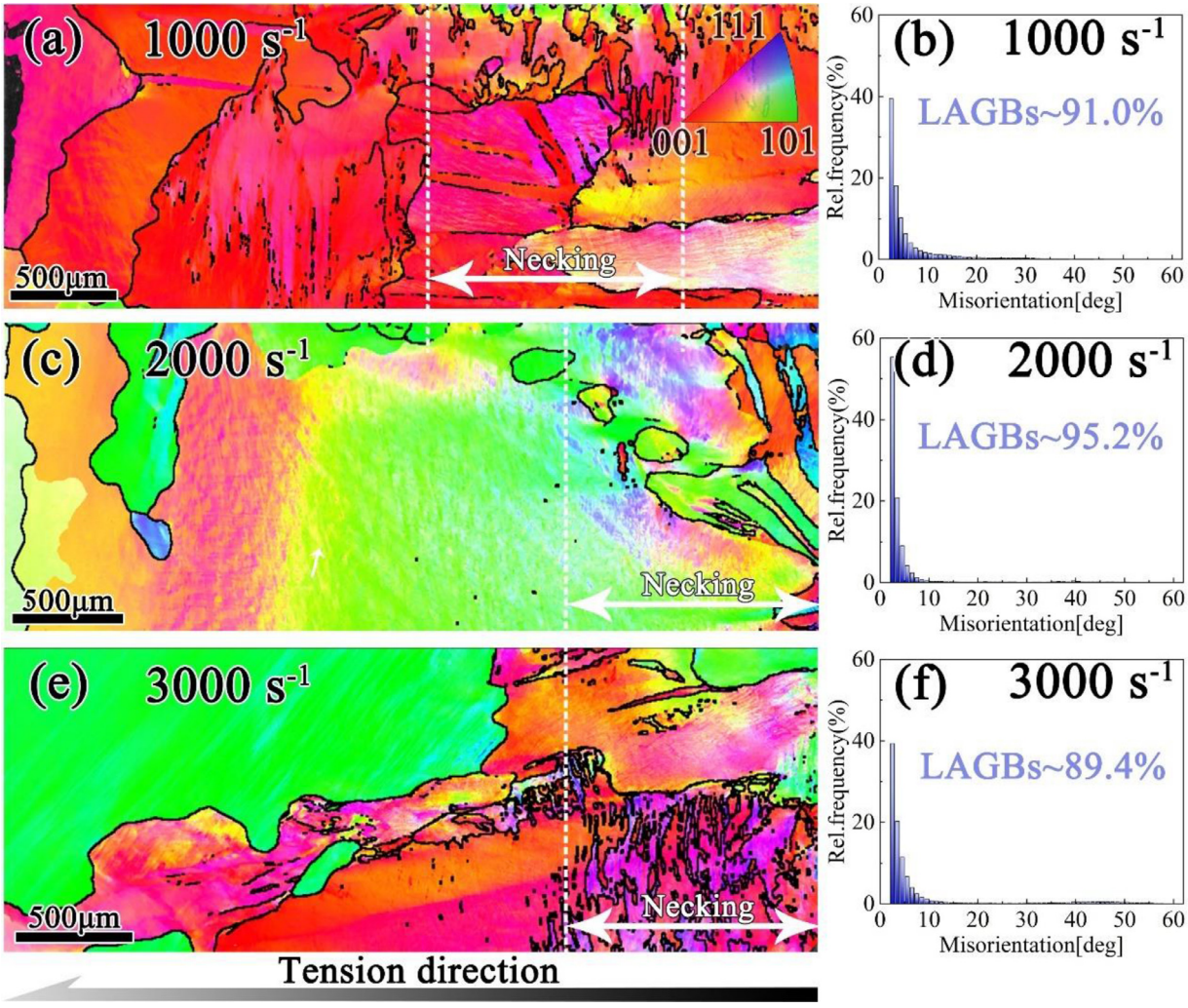

Fig. 6. IPF maps with the grain boundary (black lines outline the grain boundaries with a misorientation >15°) and the histograms of grain boundary misorientation analysis on the samples at different tensile strain rates: (a, b) 1000 s^{-1}; (c, d) 2000 s^{-1}; (e, f) 3000 s^{-1}. The black arrow indicates the tensile direction.

3.4. Slip activity during dynamic tension and compression

The active slip systems were analyzed by means of EBSD-assisted slip trace analysis in an effort to comprehend the T-C asymmetry of the MEA. Taking the sample at 2000 s^{-1} compression as an exemplar, the grain orientation is determined by IPF mapping (Fig. 9(a)). All possible slip plane traces were calculated by the in-house Spyder code using the deformed grain mean orientation and the active slip traces were distinguished by the geometrically necessary dislocation (GND) map using MATLAB code (Fig. 9(b)) [47]. The slip systems and corresponding Schmid factors are visualized in the table (Fig. 9(c)). According to the best-matched calculated and observed slip traces, the three active slip systems are marked by three arrows, corresponding to the $(11\bar{1})$ $[1\bar{1}0]$, $(\bar{1}11)$ [011] and (111) $[10\bar{1}]$ slip systems with Schmid factors of 0.49, 0.47 and 0.18, respectively. The grains in the dynamic tensile samples were analyzed according to the same method (see Fig. S6). To obtain a statistically solid conclusion, the number of the activated slip modes and their frequencies in each grain are counted in the same way under dynamic tension and compression at different strain rates. The frequency of activated slip modes together with the distribution of Schmid factors for all the samples is summarized in Fig. 9(d–f). The total frequency of Schmid factors > 0.4 in the grains with slip traces under dynamic compression is larger than that for dynamic tension at each strain rate. However, there is a reverse trend when the Schmid factors are less than 0.2. Taking the highest strain rate as an example, the total frequency is ~4% for compressive sample while the value is ~26% for tension, with regard to the Schmid factor less than 0.2.

To further quantify the dislocation density, MATLAB software with MTEX code was used. The dislocation density elevates with the increasing strain rate under both dynamic tension and compression (Fig. 10(a–f)). The dislocation density is relatively higher when closer to the slip traces. The Kernel Average Misorientation (KAM) distributions shift to an overall high value with the increasing tensile strain rate. For example, the average KAM is about 0.41° at 1000 s^{-1}, and the average KAM increases to 1.50° and 2.11° at 2000 and 3000 s^{-1}, respectively (Fig. 10(g)). By contrast, the average KAM for the compression samples slightly increases from 0.48° at 1000 s^{-1} to 0.63° at 3000 s^{-1} (Fig. 10(h)). A rough estimate of the density of GNDs ρ_{GND} can be expressed as a function of the accumulated average local misorientation angle, θ, which is retrieved directly from EBSD data [52,53]:

$$\rho_{GND} = \frac{\theta}{\mu b} \tag{6}$$

where b is the length of the Burgers vector. Taking $b = 0.254$ nm for the MEA [54,55], the step size μ (0.4 μm) and the average local misorientation angle θ (KAM) into Eq. (6), the GND den-

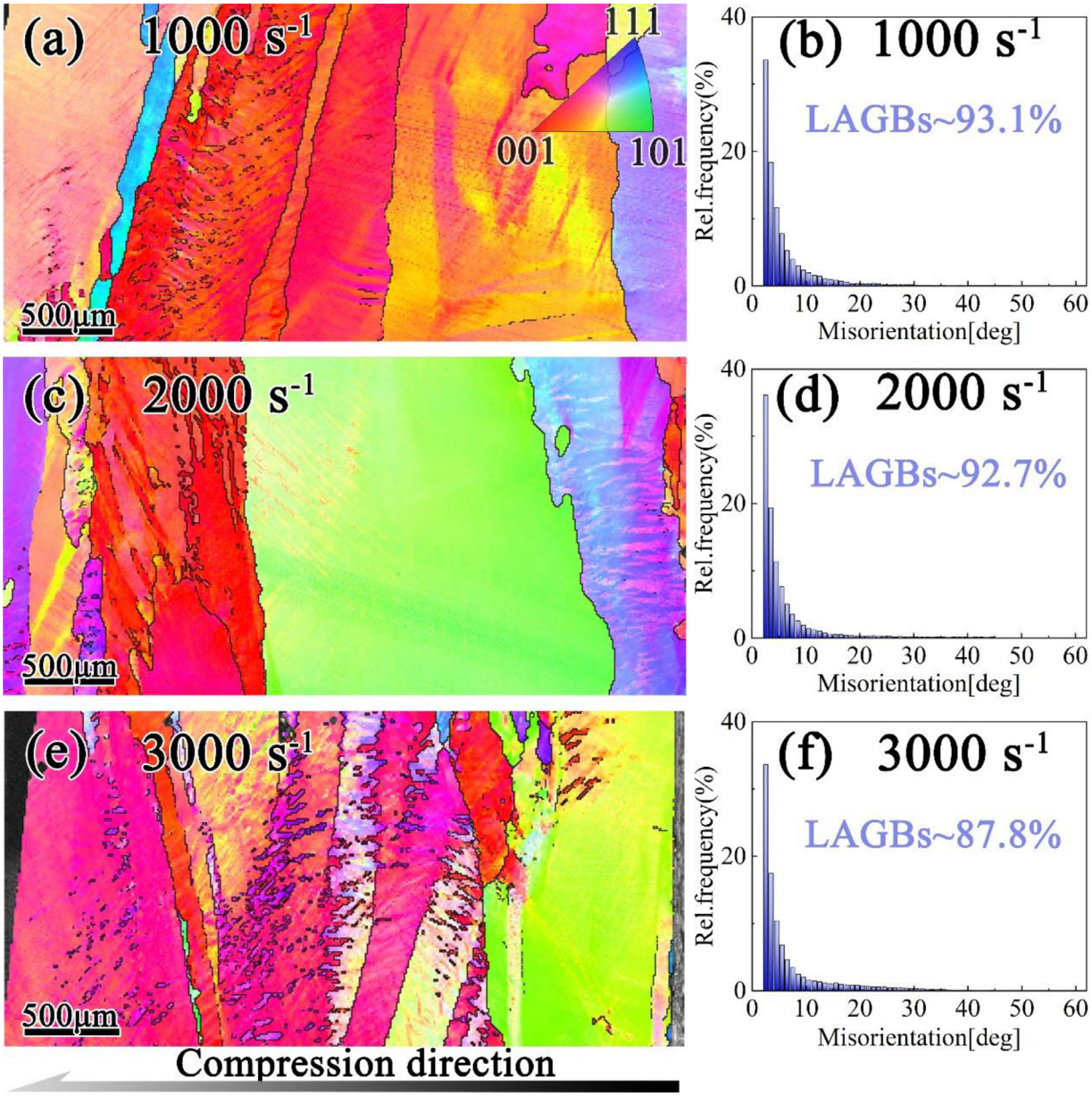

Fig. 7. IPF maps with the grain boundary (black lines mark the grain boundaries with a misorientation >15°) and the histograms of grain boundary misorientation analysis on the samples at different compressive strain rates: (a, b) 1000 s^{-1} at a strain of 0.17; (c, d) 2000 s^{-1} at a strain of 0.23; (e, f) 3000 s^{-1} at a strain of 0.33. The black arrow indicates the dynamic compression direction.

sity was calculated for each sample (Fig. 10(i)). For instance, the GND density increases from 7.05 × 10^{13} m^{-2} at 1000 s^{-1} to 2.58 × 10^{14} m^{-2} at 2000 s^{-1} and further increases by five times to 3.61 × 10^{14} m^{-2} at 3000 s^{-1} during dynamic tension. While for the compressive samples, the density increases slowly by 30.5% from 8.20 × 10^{13} m^{-2} at 1000 s^{-1} to 1.07 × 10^{14} m^{-2} at 3000 s^{-1}. Consistent with TEM results and slip trace analyses, the discrepancy of dislocation slip behavior for tension and compression plays a vital role in the T-C asymmetry of the MEA.

4. Discussion

4.1. CRSS dependent T-C asymmetry

The T-C asymmetry is closely correlated to the asymmetry in the critical resolved shear stress (CRSS) of active deformation modes (e.g., dislocation slip and twinning) between tension and compression. In our study, no twins were captured in the current MEA under either dynamic tension or compression even at very high strain rates. SFE is deemed as an intrinsic parameter in determining the competitive deformation mechanisms including slip and twinning. From the previous work, the SFE was estimated to be 50 mJ m^{-2} [54,55], much higher than that of the CoCrNi-based alloys (14–36 mJ m^{-2}) [33,35,36,40]. Dislocations with the Burgers vector, a 60°full dislocation ($b=\frac{1}{2}<110>$) are observed to be narrowly dissociated into two partial dislocations from the relatively high stacking fault energy of 50 mJ m^{-2} (Fig. 11). The critical twinning stress for extending stacking faults (τ_{twin}) can be estimated using the following equation [56]:

$$\tau_{twin} = \frac{2SFE}{b_p} \tag{7}$$

where b_p is the length of the Burgers vector of the partial dislocation (~1.466 Å) for the MEA according to the previous

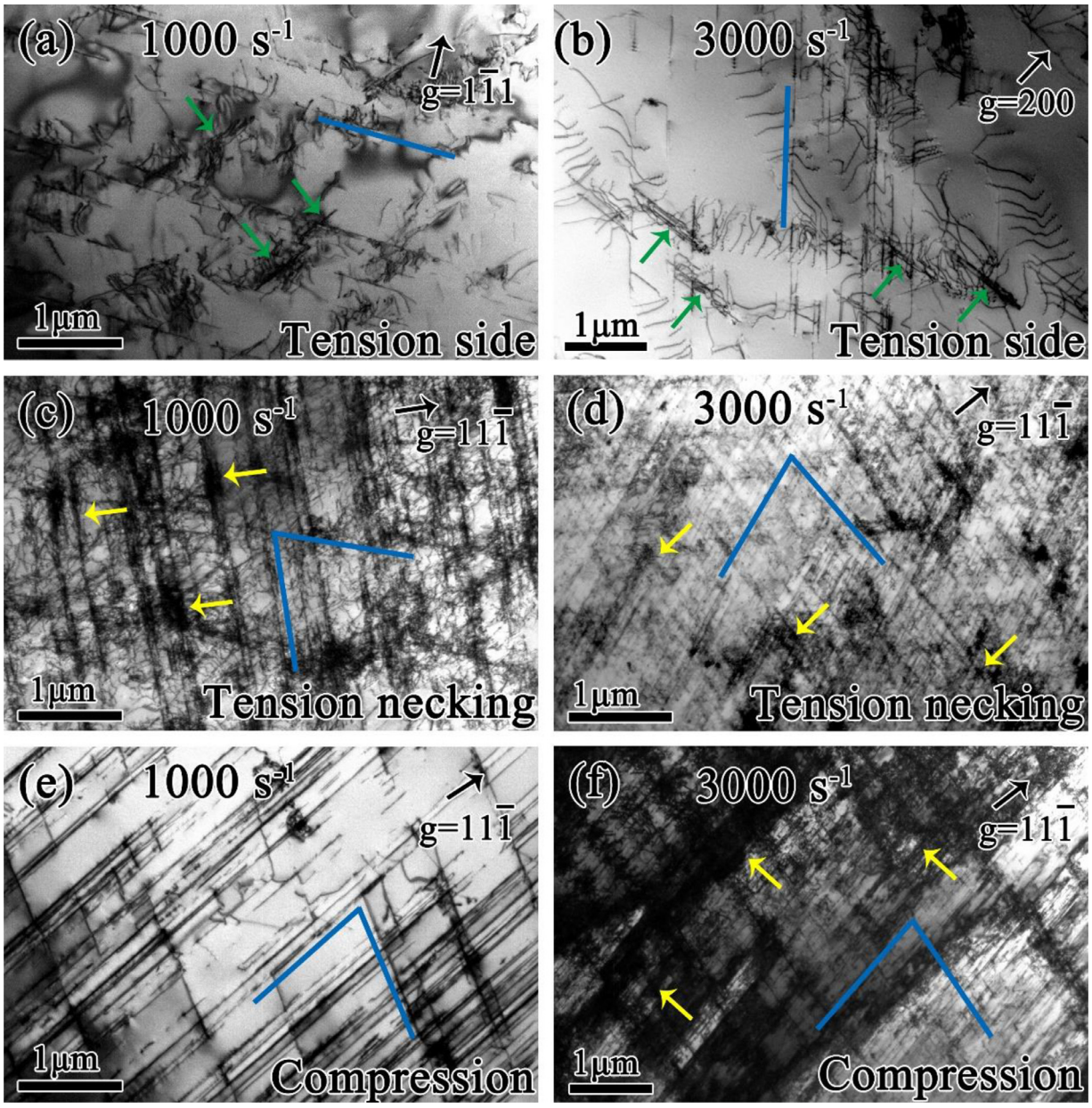

Fig. 8. Typical two-beam TEM micrographs showing the microstructure on the dynamic tension side region at (a) 1000 s^{-1} and (b) 3000 s^{-1}, tension necking region at (c) 1000 s^{-1} and (d) 3000 s^{-1}, and compression samples at (e) 1000 s^{-1} at a strain of 0.17 and (f) 3000 s^{-1} at a strain of 0.33. The green arrows, yellow arrows and blue lines indicate Lomer locks, HDDWs and slip traces, respectively. All the images are taken in the [011] zone axis with the $g = 11\bar{1}$ reflection except (a) with $g = 1\bar{1}1$ and (d) with $g = 200$ reflections.

work [54,55]. Then, the critical twinning stress is estimated to be 682 MPa, much higher than the experimentally measured value of 235 MPa for CoCrFeMnNi HEA [57]. If further converting the τ_{twin} value to normal stress via a Taylor factor of 3.06 [48], the equivalent stress for twinning can be estimated to be 2087 MPa, almost seven times as high as the estimated stress (300 MPa) for CoCrFeMnNi HEA during dynamic tension at 2100 s^{-1} [34]. This equivalent stress for twinning exceeds the alloy's ultimate tensile or compressive stress, i.e., 1355 MPa under dynamic compression at 8000 s^{-1}, and 1030 MPa under tension at 3000 s^{-1} (Figs. 3 and S5). It is therefore conceivable that the T-C asymmetry is solely dislocation slip dependent.

The slip trace analysis indicates that some hard slip modes in the grains with low Schmid factor can be activated under dynamic tension (Fig. 9), which well substantiates the observed T-C asymmetry. The yield stress is the sum of the components from all individual crystals with both hard and soft crystallographic orientations with respect to the loading axis. It is reasonable to quantitatively calculate the CRSS for dislocation slip in the MEA as follows [11,48]:

$$\tau_{CRSS} = \sigma_{yield} \cdot \bar{m} \tag{8}$$

where $\bar{m}$ is the average Schmid factor of the corresponding slip system. The value of $\bar{m}$ decreases with the elevated strain rate from 1000 s^{-1} to 3000 s^{-1} in tension, while the tendency is increasing from 1000 s^{-1} to 2000 s^{-1} and slightly decreasing in strain rate from 2000 s^{-1} to 3000 s^{-1} in compression (Fig. 12). The absolute values of CRSS at each given strain rate as well as the strain rate dependence of CRSS at dynamic tension are much larger than those under dynamic compression (Table 2). For instance, it is calculated that the $\bar{m}$ for slip is 0.333 ± 0.152 and 0.408 ± 0.114 under dynamic tension and compression at a strain rate of 2000

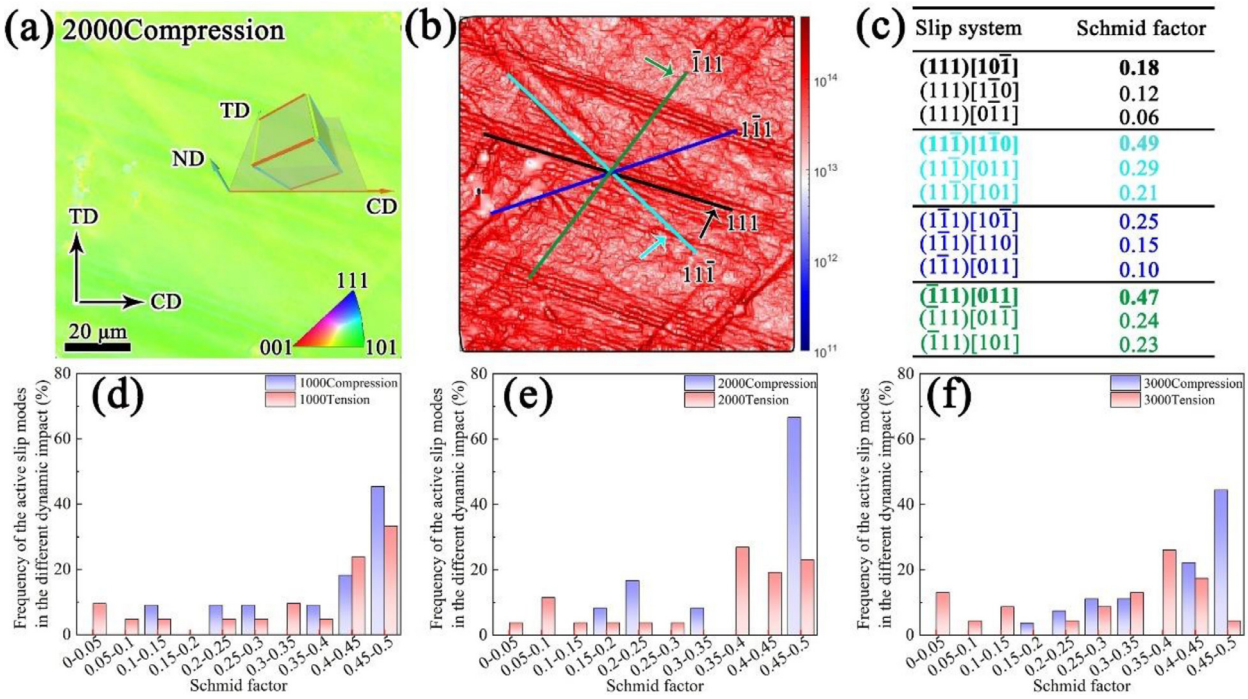

Fig. 9. Slip trace analysis for the grain after dynamic compression at the strain rate of 2000 s^{-1}: (a) IPF map of one grain with a specific orientation, ND-normal direction, CD-compression direction, TD-transverse direction; (b) Calculated GNDs map for determining the active slip traces and four distinct bold lines representing variant slip systems; (c) Slip systems with corresponding Schmid factors. In this case, the three bold fonts with the maximum Schmid factors indicated by three arrows in (b) are deemed as the active slip systems, based on the best match between calculated possible slip plane traces. (d–f) Frequency of the active slip modes and the distributions of Schmid factors in the samples under dynamic tension and compression at different strain rates: (d) 1000 s^{-1}, (e) 2000 s^{-1}, (f) 3000 s^{-1}.

Table 2
Summary of yield stresses, average Schmid factor, and CRSS of the current MEA during dynamic deformation.

Dynamic deformation	Yield stress (MPa)	Average Schmid factor	CRSS (MPa)
Tension			
1000 s^{-1}	408 ± 8	0.346 ± 0.143	141 ± 3
2000 s^{-1}	489 ± 6	0.333 ± 0.152	163 ± 2
3000 s^{-11}	510 ± 66	0.302 ± 0.139	154 ± 20
Compression			
1000 s^{-1}	340 ± 13	0.376 ± 0.120	128 ± 5
2000 s^{-1}	356 ± 20	0.408 ± 0.114	145 ± 8
3000 s^{-1}	372 ± 21	0.403 ± 0.100	150 ± 8

s^{-1}, respectively. The σ_{CRSS} is measured to be 163 ± 2 MPa in tension and 145 ± 8 MPa in compression according to the experimental value of yield stress (489 ± 6 and 356 ± 20 MPa). All these CRSS values are considerably larger than that of CoCrFeMnNi (62–90 MPa) and $Al_{0.1}$CoCrFeNi (72–79 MPa) at the same strain rate level [33–36]. This difference can be interpreted by additions of Mo and V with larger atomic radius into the MEA (the atomic size is 1.24 Å for Ni, 1.26 Å for Co, 1.27 Å for Fe, 1.35 Å for V and 1.40 Å for Mo), serving as severe lattice distortion sites and strong barriers for dislocation slip (see more discussions in Fig. S7). As pointed out in CrMnFeCoNi and NiCoFeCrAl HEAs, a relatively high Hugoniot elastic limit (HEL) and high phase transition threshold stress stem from their intrinsic chemically disordered structures and large resistance to dislocation motion [43,58]. Moreover, through molecular dynamics simulation of CoCrNi MEA, HEL along the [1$\bar{1}$0] crystal direction was lower than that of [111] direction, but this trend was reversed for pure FCC metals [58]. It was interpreted that the lattice distortion is absent and the lattice resistance to dislocation glide is relatively low in pure FCC metals, while dislocation nucleation becomes easier and propagation harder due to the existence of lattice resistance for the MEA [58]. Thus, the anisotropy in strength between dynamic tension and compression is complicated by the fact that strength is sensitive to both the amounts of dislocations and the resistance of dislocation motion. For dynamic tension, a larger number of stressed slip systems with severe lattice distortion have lower Schmid factors, in contrast to higher Schmid factors with a narrow range for dynamic compression. Above all, the resultant higher CRSS and more intensive hard slip modes in dynamic tension significantly contribute to the higher tensile yield stress, which leads to anomalous T-C asymmetry.

4.2. Strain rate hardening

As demonstrated, the yield stress significantly increases with the increasing strain rate for the current MEA under both tension and compression (Fig. 4(a)). The shear stress τ to counterbalance stresses due to the lattice resistance and the microstructure, can be decomposed into an athermal stress τ_a and an effective stress τ^* [59]:

$$\tau = \tau_a(\gamma_p) + \tau^*(T, \dot{\gamma}_p) \quad (9)$$

where τ_a is the athermal component resulting from long-range internal stresses impeding the plastic flow, γ_p is shear strain, τ^* is strain rate $\dot{\gamma}_P$ and temperature T dependent and arises from glide

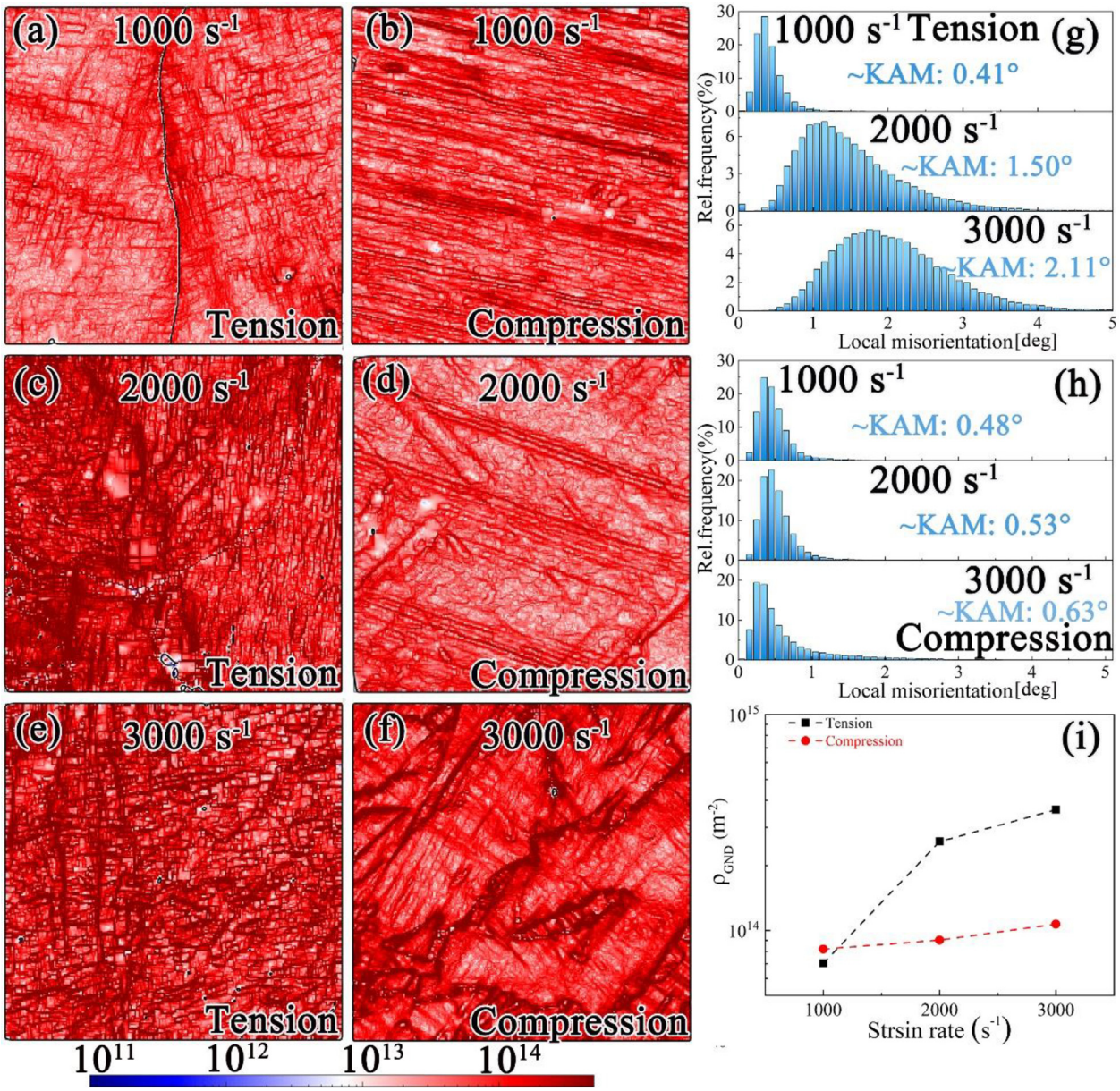

Fig. 10. GND density analysis in the tension necking region and compression center region of the sample deformed at different strain rates: (a, b) 1000 s^{-1}; (c, d) 2000 s^{-1}; (e, f) 3000 s^{-1}. The corresponding histograms of local misorientation (g, h) for the dynamic tension and compression samples. (i) Statistical value of the GND density for dynamic tension and compression samples at three different strain rates.

dislocations overcoming short-range obstacles by thermal activation. According to the model proposed by Orowan [60], the shear strain rate can be described as:

$$\dot{\gamma}_p = \rho_m b l \bar{\lambda} \nu \exp\left(-\frac{Q}{KT}\right) = \gamma_0 \exp\left(-\frac{Q_0 - \tau_{eff}\Delta V^*}{KT}\right) \quad (10)$$

where ρ_m is the mobile dislocation density, b is the magnitude of the Burgers vector, l is the length of dislocation line, ν is the vibration frequency of dislocation, $\bar{\lambda}$ is the mean free path of dislocation slip, Q is the Gibbs free activation energy, the Boltzmann factor K and T describe the probability of a successful thermal activation event, γ_0 is a pre-exponential constant, Q_0 is the Helmholtz free energy for overcoming the obstacles to dislocation motion, $\tau_{eff}\Delta V^*$ is the work done by the effective stress τ_{eff}, and ΔV^* is the effective activation volume equal to the activation area $l\bar{\lambda}$ times b. It is widely accepted that the SRS index m and activation volume are two vital parameters in evaluating the difference in strain rate hardening ability. First, the measured m is 0.21 for dynamic tension, while the value is 0.08 for dynamic compression (Fig. 13(a)). By contrast, the m values of our MEA are larger than that of the CoCrFeMnNi HEA (0.022) in dynamic tension mode [34] and the $Al_{0.1}$CoCrFeNi HEA (0.017) in dynamic compression mode [37]. In addition, the m value is one order of magnitude higher than that for the coarse-grained FCC materials ($m \leq 0.01$), indicative of strong resistance to shear fracture [61,62]. Second, the apparent activation volume (V) is related with the rate-dependent dislocation processes and can be calculated as [63,64]:

$$V = M_T K_B T \frac{\partial \ln \dot{\varepsilon}}{\partial \sigma} \quad (11)$$

where M_T is the Taylor factor, K_B is the Boltzmann's constant, σ is the normal flow stress, and $\dot{\varepsilon}$ is the normal strain rate. The estimated V of the present MEA is about 8.23 b^3 under dynamic tension, much smaller than that of dynamic compression (27.9 b^3). Taking b = 0.254 nm for the MEA into Eqs. (9) and (10), the ac-

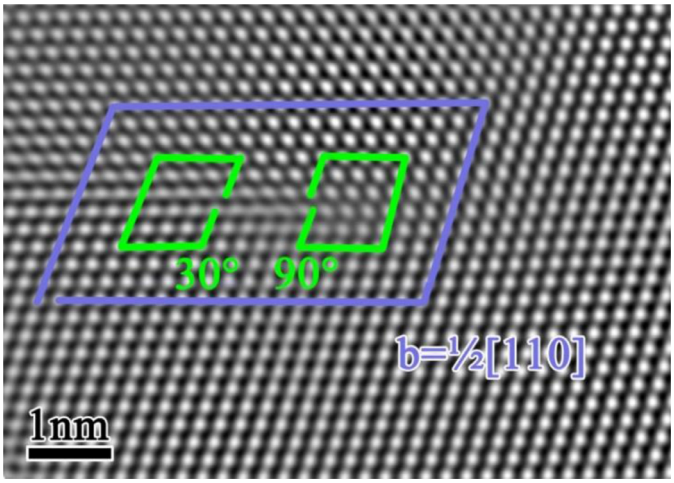

Fig. 11. An HRTEM image taken with the $Z = [110]$ zone axis, showing the atomic structure of a 60° full dislocation, with the Burgers vector b of $\frac{1}{2}[110]$. This 60° dislocation is dissociated into a 30° partial and a 90° partial. The distance between the two partials is the stacking fault width, which is as small as about 1 nm.

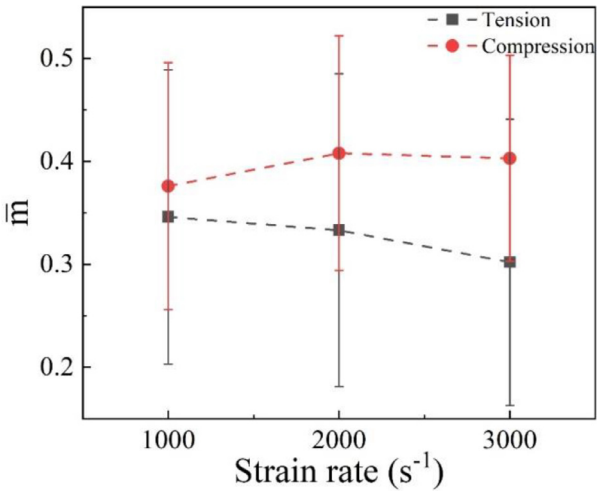

Fig. 12. Variations of the average Schmid factor with respect to the strain rate for the current MEA under dynamic tension and compression.

tivation area is calculated to be about 27.9 b^2, and the mean free path of dislocation slip $\bar{\lambda}$ is 5.28b (1.34 nm) for the MEA during dynamic compression. While the activation area and $\bar{\lambda}$ decrease to 8.23 b^2 and 2.87b (0.73 nm), respectively, for dynamic tension. $\bar{\lambda}$ indicates the distance between the obstacles. The smaller $\bar{\lambda}$ for dynamic tension will bring about extremely heavy piling-up of mobile dislocation and dislocation reactions as well as multiplications, contributing to the higher flow stress. It is consistent with the smaller spacing of the planar slip bands and higher dislocation density. The spacing decreases with the elevated strain rate from 1000 s^{-1} to 3000 s^{-1} in both tension and compression, while the reduction rate is quicker in tension than compression (Fig. 13(b)). Previous investigations indicate that the low activation volume after yielding reflects the interaction of dislocations with solutes, ascribed to the short-range effects such as lattice distortion and short-range ordering [65]. The rate-dependent deformation mechanism is dislocation slip against nanoscale inhomogeneities such as short-range ordering or local chemical fluctuations with pile-up stresses [41,66,67]. These effects in turn facilitate planar slip and formation of confined dislocations in narrow planar bands. Therefore, it requires higher stress for the onset of dislocation motion at high strain rates, which leads to a significant rise in yield strength.

4.3. Dynamic strain hardening

In despite of the diverse trends of strain hardening exponent (n) with respect to the increasing strain rate, the present MEA still shows excellent dynamic strain hardening in the strain rate range between 1000 and 3000 s^{-1}, as shown in Fig. 4(c). The current study demonstrates the MEA possesses noticeably large dislocation storage capability and high n values (1.15–1.47), greater than that of extensively investigated CoCrFeMnNi (0.85), $Al_{0.6}$CoCrFeNi (0.71) and conventional steels (0.56–0.78) [26,31,68]. In the literature, the extra strain hardening was interpreted to stem from TRIP and TWIP effects in homogenous materials [69], or hetero-deformation induced hardening in hetero-structured materials [70]. While for the current MEA, planar dislocation slip governs dynamic deformation, bringing about plenty of planar dislocations, Lomer dislocation locks and HDDWs within the coarse grains. These piled-up dislocations are strong barriers in obstructing dislocation motion and thus produce large back forces. First, sessile Lomer dislocation locks, edge ⟨110⟩ {001} dislocations (Fig. 8), could act as the Frank-Read sources for dislocation multiplication by forming parallel and long dislocations along the same slip systems at the early stage of dynamic tension. It was suggested that large non-planar strain field around the dislocation core of the sessile Lomer locks can also greatly hamper the free movement of dislocations [51]. It is reasonable that more Lomer locks are initiated in the beginning of dynamic tension than compression, in proportion to the measured dislocation density. Second, it should be noted that the slip bands become longer and denser and their interval spacing decreases gradually with the increasing strain rate (Figs. 8 and 13). Under such circumstances, more and more intersected slip bands and mobile dislocations act as Frank-Read sources to multiplicate new {111} slips with increasing stress or strain. Both the nano-scale interval of slip planes and the heavy pile-ups of high-density dislocations on each slip plane produce the farthest dislocation accumulation and reactions as well as strain hardening during dynamic deformation. Third, the activation barriers created by lattice friction, short-range order or local chemical fluctuations for dislocation slip are expected to be strong in the current MEA by adding large atoms. It remains unclear whether the solid solution hardening is sensitive to the loading direction.

The strain hardening rate is higher under dynamic tension than compression in the work hardening stage II (Fig. 3), which can be explained by the following two aspects. First, the spacing of the planar slip bands is narrower in tension than compression at the same stain rate, for instance, 31 ± 17 and 64 ± 26 nm for tension and compression at the strain rate of 3000 s^{-1}, respectively (Fig. 13). It was suggested that the superior mechanical properties can be enabled by dynamic slip band refinement in high-Mn lightweight steel [71]. Second, more hard slip modes in the grains with low Schmid factor can be activated under dynamic tension rather than dynamic compression. A recent paper pointed out that dislocation multiplication in inactive slip systems can contribute significantly to strain hardening, similar to that in active systems [72]. This can be verified by the higher GND density (3.61×10^{14} m^{-2} at 3000 s^{-1}) in tension compared to that in compression (1.07×10^{14} m^{-2} at 3000 s^{-1}).

4.4. Origins of T-C asymmetry

Our microstructural analysis confirms that the atypical T-C asymmetry is solely related to the dislocation slip processes in the current MEA during dynamic loading. More hard slip modes are activated in grains under dynamic tension than under compression. In the absence of twins and phase transitions, the dislocation slip governed T-C asymmetry is illustrated in Fig. 14. Three main factors are taken into account. First, the CRSS is higher, and more hard

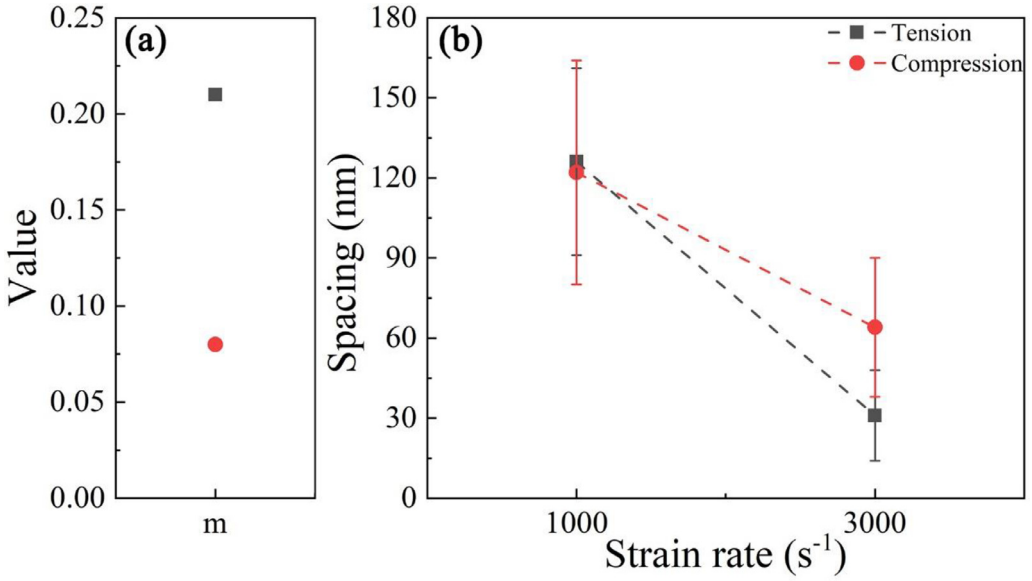

Fig. 13. (a) Value of SRS (m) for dynamic tension and compression, (b) variations of the average spacing of planar slip bands with respect to the strain rate for the current MEA.

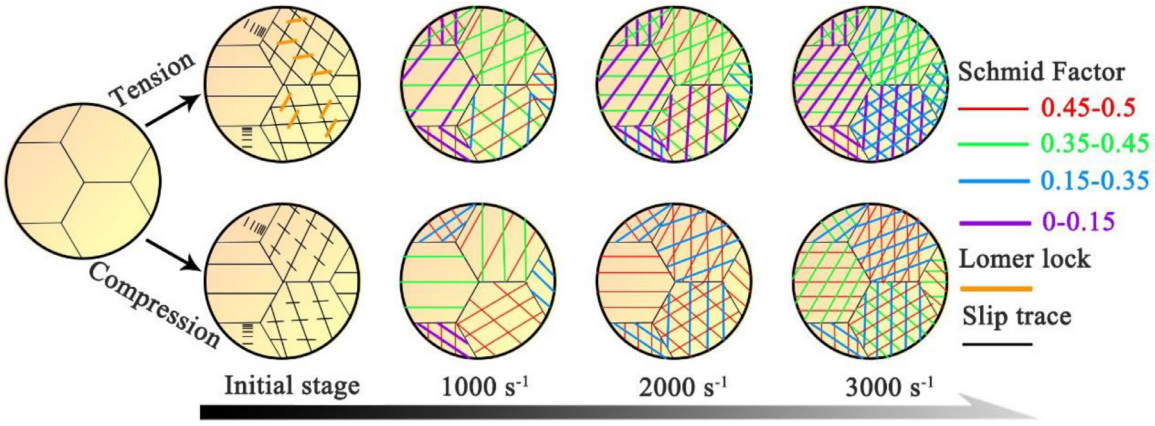

Fig. 14. Schematic illustration showing the deformation microstructure evolution of the $Ni_2CoFeV_{0.5}Mo_{0.2}$ MEA under dynamic tension and compression at different strain rates. The slip traces with corresponding Schmid factors are represented by different color lines. In this case, the red lines (0.45–0.5), green lines (0.35–0.45), blue lines (0.15–0.35), and purple lines (0–0.15) indicate the range of Schmid factors. The Lomer locks and active dislocation slip are indicated by the orange and black lines, respectively.

slip modes are operative in dynamic tension, giving rise to higher yield stress. In addition, the total frequency of grains exhibiting more slip traces for tension exceeds that for compression, in accordance with the trend for the dislocation density. Second, at the initial stage, larger amounts of immobile Lomer locks under dynamic tension are of paramount importance to the stronger yield stress. Third, the measured SRS value is three times for dynamic tension (0.21) than compression (0.08), leading to much larger flow strength in the MEA. The smaller spacing of planar slip bands also contributes to the larger flow stress in dynamic tension.

5. Conclusions

The dynamic tensile and compressive behaviors of the FCC $Ni_2CoFeV_{0.5}Mo_{0.2}$ MEA samples were thoroughly researched in the strain rate ranging from 1000 s^{-1} to 3000 s^{-1} at room temperature. A pronounced dislocation mediated T-C asymmetry was uncovered, and the salient conclusions can be drawn as follows:

(1) Under dynamic tension, the yield strength elevates by 25% from 408 ± 8 MPa at 1000 s^{-1} to 510 ± 66 MPa at 3000 s^{-1}, respectively. While for dynamic compression, the yield strength increases by 9.4% from 340 ± 13 MPa at 1000 s^{-1} to 372 ± 21 MPa at 3000 s^{-1}. The dynamic tensile strength exceeds the compressive strength and their discrepancy increases from 50 MPa to 280 MPa within the strain rate from 1000 s^{-1} to 3000 s^{-1} at a strain of 0.17.

(2) Exhaustive TEM and EBSD characterizations confirm that dislocation slip is the sole deformation mechanism for both dynamic tension and compression. During dynamic tension, the immobile Lomer locks occur at the early stage accompanied by parallel slip trace lines, while only parallel slip trace lines are activated under dynamic compression. The higher strain rate gives rise to a tendency toward more planar networks and smaller spacing of the planar slip bands. Compared to dynamic compression, dynamic tension brings about smaller spacing between planar slip bands and higher dislocation density in the current MEA.

(3) The MEA possesses noticeably high dislocation storage capability (n: 1.15–1.47). Three factors may account for the high strain hardening rate. First, additions of Mo and V with larger atomic radius into the MEA are supposed to produce high solid solution hardening. Second, plenty of planar dislocations, Lomer dislocation locks and HDDWs are formed within the coarse

grains, facilitating dislocation intersections and multiplication. Third, the spacing between planar slip bands decreases significantly with the increasing strain rate, effectively impeding dislocation slip.

(4) The uncommon dynamic tension-compression asymmetry is plausibly interpreted by higher CRSS and more hard slip modes (lower average Schmid factor) activated in grains under dynamic tension than under compression. Larger strain rate sensitivity (SRS) is responsible for the higher flow strength, ascribed to the occurrence of more Lomer-locks, narrower spacing of planar slip bands and higher dislocation density under dynamic tension. The current study may provide a thorough understanding to support materials design under severe loading conditions, such as crash or impact.

Declaration of competing interest

The authors declare that they have no known competing financial interests or personal relationships that could have appeared to influence the work reported in this paper.

Acknowledgements

Y.H. Zhao acknowledges the financial support from the National Key R&D Program of China (No. 2017YFA0204403), the National Natural Science Foundation of China (Nos. 51971112 and 51225102), and the Fundamental Research Funds for the Central Universities (No. 30919011405). X. Chen would like to acknowledge the financial support from the National Natural Science Foundation of China (Nos. 52001165 and 51931003), the Natural Science Foundation of Jiangsu Province, China (No. BK20200475), and the Fundamental Research Funds for the Central Universities (No. 30921011215). The authors are thankful for the technical support from Jiangsu Key Laboratory of Advanced Micro&Nano Materials and Technology, and the Materials Characterization Facility of Nanjing University of Science and Technology.

Supplementary materials

Supplementary material associated with this article can be found, in the online version, at doi:10.1016/j.jmst.2023.02.051.

References

[1] O. Cazacu, I.R. Ionescu, J.W. Yoon, Int. J. Plast. 26 (2010) 887–904.
[2] S.M. Yin, C.H. Wang, Y.D. Diao, S.D. Wu, S.X. Li, J. Mater. Sci. Technol. 27 (2011) 29–34.
[3] Y.Q. Chi, X.H. Zhou, X.G. Qiao, H.G. Brokmeier, M.Y. Zheng, Mater. Des. 170 (2019) 107705.
[4] Q. Yu, L. Qi, R.K. Mishra, J. Li, A.M. Minor, Proc. Natl. Acad. Sci. U. S. A. 110 (2013) 13289–13293.
[5] Z. Leng, H. Pan, C. Guo, Z. Wang, G. Zou, F. Jiang, Mater. Sci. Eng. A 667 (2016) 468–472.
[6] M. Baral, T. Hama, E. Knudsen, Y.P. Korkolis, Int. J. Plast. 105 (2018) 164–194.
[7] H. Zhou, H.Y. Ning, X.L. Ma, D.D. Yin, L.R. Xiao, X.C. Sha, Y.D. Yu, Q.D. Wang, Y.S. Li, J. Mater. Sci. Technol. 34 (2018) 1067–1075.
[8] D.D. Yin, C.J. Boehlert, L.J. Long, G.H. Huang, H. Zhou, J. Zheng, Q.D. Wang, Int. J. Plast. 136 (2021) 102878.
[9] S.-.H. Kim, S.W. Lee, B.G. Moon, H.S. Kim, S.H. Park, J. Mater. Sci. Technol. 46 (2020) 225–236.
[10] S. Xu, T. Liu, H. Chen, Z. Miao, Z. Zhang, W. Zeng, Mater. Sci. Eng. A 565 (2013) 96–101.
[11] Z.W. Huang, S.B. Jin, H. Zhou, Y.S. Li, Y. Cao, Y.T. Zhu, Int. J. Plast. 112 (2019) 52–67.
[12] A. Meng, X. Chen, J. Nie, L. Gu, Q. Mao, Y. Zhao, J. Alloy. Compd. 859 (2021) 158222.
[13] P. Lin, Y. Hao, B. Zhang, S. Zhang, C. Chi, J. Shen, Mater. Sci. Eng. A 707 (2017) 172–180.
[14] Q. Li, S. Xue, Y. Zhang, X. Sun, H. Wang, X. Zhang, Int. J. Plast. 132 (2020) 102760.
[15] G.G. Yapici, I.J. Beyerlein, I. Karaman, C.N. Tomé, Acta Mater. 55 (2007) 4603–4613.
[16] J. Joseph, N. Stanford, P. Hodgson, D.M. Fabijanic, Scr. Mater. 129 (2017) 30–34.
[17] X. An, Z. Wang, S. Ni, M. Song, Sci. China Mater. 63 (2020) 1797–1807.
[18] B. Gludovatz, A. Hohenwarter, D. Catoor, E.H. Chang, E.P. George, R.O. Ritchie, Science 345 (2014) 1153–1158.
[19] B. Gludovatz, A. Hohenwarter, K.V. Thurston, H. Bei, Z. Wu, E.P. George, R.O. Ritchie, Nat. Commun. 7 (2016) 10602.
[20] X.J. Fan, R.T. Qu, Z.F. Zhang, J. Mater. Sci. Technol. 123 (2022) 70–77.
[21] J.Y. He, H. Wang, H.L. Huang, X.D. Xu, M.W. Chen, Y. Wu, X.J. Liu, T.G. Nieh, K. An, Z.P. Lu, Acta Mater. 102 (2016) 187–196.
[22] X. Gao, Y. Lu, B. Zhang, N. Liang, G. Wu, G. Sha, J. Liu, Y. Zhao, Acta Mater. 141 (2017) 59–66.
[23] X. Liu, Y. Wu, Y. Wang, J. Chen, R. Bai, L. Gao, Z. Xu, W.Y. Wang, C. Tan, X. Hui, J. Mater. Sci. Technol. 127 (2022) 164–176.
[24] P. Shi, Y. Li, Y. Wen, Y. Li, Y. Wang, W. Ren, T. Zheng, Y. Guo, L. Hou, Z. Shen, Y. Jiang, J. Peng, P. Hu, N. Liang, Q. Liu, P.K. Liaw, Y. Zhong, J. Mater. Sci. Technol. 89 (2021) 88–96.
[25] X. Kong, Y. Liu, M. Chen, T. Zhang, Q. Wang, F. Wang, J. Mater. Sci. Technol. 105 (2022) 142–152.
[26] X. Gao, Y. Lu, J. Liu, J. Wang, T. Wang, Y. Zhao, Materialia 8 (2019) 100485.
[27] Z. Li, K.G. Pradeep, Y. Deng, D. Raabe, C.C. Tasan, Nature 534 (2016) 227–230.
[28] D. Wei, X. Li, S. Schönecker, J. Jiang, W.-.M. Choi, B.-.J. Lee, H.S. Kim, A. Chiba, H. Kato, Acta Mater. 181 (2019) 318–330.
[29] Y. Qi, T. Cao, H. Zong, Y. Wu, L. He, X. Ding, F. Jiang, S. Jin, G. Sha, J. Sun, J. Mater. Sci. Technol. 75 (2021) 154–163.
[30] D.D. Zhang, H. Wang, J.Y. Zhang, H. Xue, G. Liu, J. Sun, J. Mater. Sci. Technol. 87 (2021) 184–195.
[31] L. Wang, J.W. Qiao, S.G. Ma, Z.M. Jiao, T.W. Zhang, G. Chen, D. Zhao, Y. Zhang, Z.H. Wang, Mater. Sci. Eng. A 727 (2018) 208–213.
[32] W. Jiang, X. Gao, Y. Guo, X. Chen, Y. Zhao, Mater. Sci. Eng. A 824 (2021) 141858.
[33] S.-.P. Tsai, Y.-.T. Tsai, Y.-.W. Chen, P.-.J. Chen, P.-.H. Chiu, C.-.Y. Chen, W.-.S. Lee, J.-.W. Yeh, J.-.R. Yang, Mater. Charact. 147 (2019) 193–198.
[34] J. He, Q. Wang, H. Zhang, L. Dai, T. Mukai, Y. Wu, X. Liu, H. Wang, T.-.G. Nieh, Z. Lu, Sci. Bull. 63 (2018) 362–368.
[35] J.M. Park, J. Moon, J.W. Bae, M.J. Jang, J. Park, S. Lee, H.S. Kim, Mater. Sci. Eng. A 719 (2018) 155–163.
[36] N. Kumar, Q. Ying, X. Nie, R.S. Mishra, Z. Tang, P.K. Liaw, R.E. Brennan, K.J. Doherty, K.C. Cho, Mater. Des. 86 (2015) 598–602.
[37] S. Gangireddy, L. Kaimiao, B. Gwalani, R. Mishra, Mater. Sci. Eng. A 727 (2018) 148–159.
[38] S. Gangireddy, B. Gwalani, K. Liu, R. Banerjee, R.S. Mishra, Mater. Sci. Eng. A 734 (2018) 42–50.
[39] D.L. Foley, S.H. Huang, E. Anber, L. Shanahan, Y. Shen, A.C. Lang, C.M. Barr, D. Spearot, L. Lamberson, M.L. Taheri, Acta Mater. 200 (2020) 1–11.
[40] S. Zhao, Z. Li, C. Zhu, W. Yang, Z. Zhang, D.E.J. Armstrong, P.S. Grant, R.O. Ritchie, M.A. Meyers, Sci. Adv. 7 (2021) eabb3108.
[41] T.W. Zhang, S.G. Ma, D. Zhao, Y.C. Wu, Y. Zhang, Z.H. Wang, J.W. Qiao, Int. J. Plast. 124 (2020) 226–246.
[42] Y.H. Jo, D.G. Kim, M.C. Jo, K.Y. Doh, S.S. Sohn, D. Lee, H.S. Kim, B.J. Lee, S. Lee, J. Alloy. Compd. 785 (2019) 1056–1067.
[43] Z.J. Jiang, J.Y. He, H.Y. Wang, H.S. Zhang, Z.P. Lu, L.H. Dai, Mater. Res. Lett. 4 (2016) 226–232.
[44] Y. Qiao, Y. Chen, F.-.H. Cao, H.-.Y. Wang, L.-.H. Dai, Int. J. Impact Eng. 158 (2021) 104008.
[45] W.-.R. Jian, Z. Xie, S. Xu, X. Yao, I.J. Beyerlein, Scr. Mater. 209 (2022) 114379.
[46] T. Suo, Y.-.L. Li, K. Xie, F. Zhao, K.-.S. Zhang, Q. Deng, Mech. Mater. 43 (2011) 111–118.
[47] F. Bachmann, R. Hielscher, H. Schaeben, Solid State Phenom. 160 (2010) 63–68.
[48] T.H. Courtney, in: Mechanical Behavior of Materials, Second ed, McGrawHill, New York, 2005, p. 159.
[49] H. Kim, J. Park, Y. Ha, W. Kim, S.S. Sohn, H.S. Kim, B.-.J. Lee, N.J. Kim, S. Lee, Acta Mater. 96 (2015) 37–46.
[50] Z. Wang, T. Zhang, E. Tang, R. Xiong, Z. Jiao, J. Qiao, Appl. Phys. Lett. 119 (2021) 201901.
[51] X.D. Xu, P. Liu, Z. Tang, A. Hirata, S.X. Song, T.G. Nieh, P.K. Liaw, C.T. Liu, M.W. Chen, Acta Mater. 144 (2018) 107–115.
[52] X. Chen, R. Schneider, P. Gumbsch, C. Greiner, Acta Mater. 161 (2018) 138–149.
[53] Y. Liu, Y. Cao, Q. Mao, H. Zhou, Y. Zhao, W. Jiang, Y. Liu, J.T. Wang, Z. You, Y. Zhu, Acta Mater. 189 (2020) 129–144.
[54] L. Jiang, Y.P. Lu, M. Song, C. Lu, K. Sun, Z.Q. Cao, T.M. Wang, F. Gao, L.M. Wang, Scr. Mater. 165 (2019) 128–133.
[55] W. Jiang, S. Yuan, Y. Cao, Y. Zhang, Y. Zhao, Acta Mater. 213 (2021) 116982.
[56] T.S. Byun, Acta Mater. 51 (2003) 3063–3071.
[57] G. Laplanche, A. Kostka, O.M. Horst, G. Eggeler, E.P. George, Acta Mater. 118 (2016) 152–163.
[58] Z. Xie, W.-.R. Jian, S. Xu, I.J. Beyerlein, X. Zhang, Z. Wang, X. Yao, Acta Mater. 221 (2021) 117380.
[59] D. Caillard, J.L. Martin, in: Thermally Activated Mechanisms in Crystal Plasticity, Pergamon, Amsterdam, 2003, p. 13.
[60] G.E. Dieter, in: Mechanical Metallurgy, Third ed, McGrawHill, Boston, 1986, p. 173.
[61] Q. Wei, S. Cheng, K.T. Ramesh, E. Ma, Mater. Sci. Eng. A 381 (2004) 71–79.
[62] C. Sun, J. Ma, Y. Yang, K.T. Hartwig, S.A. Maloy, H. Wang, X. Zhang, Mater. Sci. Eng. A 597 (2014) 415–421.
[63] L. Xiao, P. Huang, F. Wang, J. Mater. Sci. Technol. 86 (2021) 251–259.
[64] S. Wei, Y. Zhao, J.-.I. Jang, U. Ramamurty, J. Mater. Sci. Technol. 120 (2022) 253–264.

[65] M. Komarasamy, N. Kumar, R.S. Mishra, P.K. Liaw, Mater. Sci. Eng. A 654 (2016) 256–263.
[66] S.I. Hong, J. Moon, S.K. Hong, H.S. Kim, Mater. Sci. Eng. A 682 (2017) 569–576.
[67] J. Moon, S.I. Hong, J.W. Bae, M.J. Jang, D. Yim, H.S. Kim, Mater. Res. Lett. 5 (2017) 472–477.
[68] M.M. Wang, C.C. Tasan, D. Ponge, D. Raabe, Acta Mater. 111 (2016) 262–272.
[69] V. Shterner, I.B. Timokhina, H. Beladi, Mater. Sci. Eng. A 669 (2016) 437–446.
[70] X. Wu, M. Yang, F. Yuan, G. Wu, Y. Wei, X. Huang, Y. Zhu, Proc. Natl. Acad. Sci. U. S. A. 112 (2015) 14501–14505.
[71] E. Welsch, D. Ponge, S.M. Hafez Haghighat, S. Sandlöbes, P. Choi, M. Herbig, S. Zaefferer, D. Raabe, Acta Mater. 116 (2016) 188–199.
[72] L.A. Zepeda-Ruiz, A. Stukowski, T. Oppelstrup, N. Bertin, N.R. Barton, R. Freitas, V.V. Bulatov, Nat. Mater. 20 (2021) 315–320.